Relationship Between Lamellar Structure and Elastic Modulus of Thermally Sprayed Thermal Barrier Coatings with Intra-splat Cracks

Guang-Rong Li, Bo-Wen Lv, Guan-Jun Yang, Wei-Xu Zhang, Cheng-Xin Li, and Chang-Jiu Li

(Submitted February 7, 2015; in revised form July 15, 2015)

The elastic modulus of plasma-sprayed top coating plays an important role in thermal cyclic lifetime of thermally sprayed thermal barrier coatings (TBCs), since the thermal stress is determined by the substrate/coating thermal mismatch and the elastic modulus of top coating. Consequently, much attention had been paid to understanding the relationship between elastic modulus and lamellar structure of top coating. However, neglecting the intra-splat cracks connected with inter-splat pores often leads to poor prediction in in-plane modulus. In this study, a modified model taking account of intra-splat cracks and other main structural characteristics of plasma-sprayed yttria-stabilized zirconia coating was proposed. Based on establishing the relationship between elastic modulus and structural parameters of basic unit, effects of structural parameters on the elastic modulus of coatings were discussed. The predicted results are well consistent with experimental data on coating elastic modulus in both out-plane direction and in-plane direction. This study would benefit the further comprehensive understanding of failure mechanism of TBCs in thermal cyclic condition.

1. Introduction

Thermally sprayed ceramic coatings are widely used as thermal barrier coatings (TBCs) in both aircraft engines and land-based gas turbines due to their thermal insulating and erosion alleviating performance at high temperature. TBCs generally consist of a bond-coat with excellent oxidation resistance and a top-coat with a high thermal insulating performance. The bond-coat is typically made

Guang-Rong Li, Guan-Jun Yang, Cheng-Xin Li, and **Chang-Jiu Li**, State Key Laboratory for Mechanical Behavior of Materials, School of Materials Science and Engineering, Xi'an Jiaotong University, Xi'an 710049, Shaanxi, People's Republic of China; and **Bo-Wen Lv** and **Wei-Xu Zhang**, State Key Laboratory for Strength and Vibration of Mechanical Structures, School of Aerospace, Xi'an Jiaotong University, Xi'an 710049, Shaanxi, People's Republic of China. Contact e-mails: ygj@mail.xjtu.edu.cn, zhangwx@mail.xjtu.edu.cn, and licj@mail.xjtu.edu.cn.

of MCrAlY (M = Ni, Co, NiCo, CoNi) alloy or NiAl-based intermetallics to mitigate essentially the spallation failure of TBCs. At operating conditions, high-temperature exposure results in the formation of thermally grown oxide between the top-coat and bond-coat, which serves as an oxygen ionic diffusion barrier to retard the further oxidation of bond-coat (Ref 1-5). For the top-coat, a preferred choice is yttria-stabilized zirconia (YSZ) due to its desirable comprehensive properties: low thermal conductivity, relatively high thermal expansion coefficient (leading to a relatively low thermal mismatch between the top-coat and superalloy substrate), and favorable mechanical performance such as high toughness. Currently, two most popular techniques, namely plasma spraying (PS) and electron-beam physical vapor deposition (EB-PVD), are widely employed to deposit the YSZ top-coat. The PS still occupies a dominant position due to its features of fast, flexibility, and low cost as well (Ref 6-8).

PS ceramic coatings are formed by lamellar splats resulting from molten droplet impacting, flattening, rapid solidification, and finally lying nearly parallel to the substrate (Ref 9, 10). Three types of pores, namely globular pores, inter-splat pores, and intra-splat cracks, can be found in PS ceramic coatings, as shown in Fig. 1 presented with (a) fractured cross section and (b) surface of a splat. The inter-splat pores generally with an in-plane orientation (parallel to substrate) result from imperfect bonding between lamellar splats (Ref 11, 12). Intra-splat cracks running through the thickness of individual splats are originated from quenching stress (Ref 11, 12). Large globular voids arise from incomplete filling of molten

droplets into the rough surface of the prior deposit (Ref 13). This complex porous microstructure leads to low thermal conductivity, low stiffness, and high strain tolerance for PS ceramic coating. The elastic modulus of the PS ceramic coating shows significant anisotropy due to the above-mentioned complex porous structure. Compared with dense zirconia with a Young's modulus of 200-220 GPa (Ref 14, 15), the out-plane modulus of PS-YSZ coating is often 1/10-1/5, while the in-plane modulus is often 1/4-1/2 (Ref 14, 16-22). Because the stored elastic strain energy release rate, which determines the spallation lifetime of TBCs when reaching to or over the critical strain energy release rate (G_{ic}), is directly proportional to the in-plane modulus of top-coat under a given strain (Ref 23), it is of great significance to obtain a low elastic modulus and retain this low modulus for a long thermal exposure duration. Therefore, it becomes more necessary and challenging towards the development of high performance and durable TBCs to achieve further deeper understanding of the relationship between microstructure and elastic modulus.

There have been several papers oriented to establishing models to predict elastic modulus with three types of

Fig. 1 Porous coating structure of PS ceramic coatings (Ref 24). (a) Three types of voids in fractured cross section of PS-YSZ. (b) Intra-splat cracks in plane-view

voids, i.e. globular voids, inter-splat pores, and intra-splat cracks. Kroupa et al. (Ref 25) reported an analytical model for the plasma-sprayed ceramic coatings by inserting the three types of pores in an isotropic and homogeneous dense material. Their predicted results showed that the coating modulus in in-plane direction is related to overall porosity and out-plane crack density, while the coating modulus in out-plane direction is related to overall porosity and in-plane crack density. This model clearly shows the dependence of coating modulus on the corresponding perpendicular pores. Based on this model, Sevostianov et al. (Ref 26) further introduced a scattering factor for pore orientation and gave a better explanation on the anisotropy of elastic behavior. The pores in the above-mentioned analytical models are artificially inserted.

In order to further reveal more real pore characteristics (such as size distribution and location distribution), finite element modeling (FEM) was employed as an alternative method to predict elastic modulus of PS TBCs (Ref 27, 28). The finite element model formed from cross section images of coatings was directly applied. There is no doubt that FEM can deal with the irregular pore shape, pore-size distribution, and location distribution, which are limited by analytical models because of the complexity of pore structure.

The common characteristic of the above-mentioned methods is the isolated pore structure in a continuous material. However, PS ceramic coatings possess a continuous pore structure in a continuous material, since most of inter-splat pores and intra-splat cracks are connected to each other. This is why the PS ceramic coatings present a poor corrosion resistance (Ref 29-34) and a poor gas tightness (Ref 35-39). However, this important intrinsic characteristic of PS ceramic coatings has not been taken into account in the above-mentioned methods.

In order to understand the essential role of connected pore structure on the coating modulus, models based on the connection between inter-splat pores and intra-splat cracks have to be developed. Based on lamellar structure, Li et al. (Ref 40) proposed a structural model by disk-shaped splats stacking with limited bonding area. Compared to the methods in the former paragraphs, this model presented a structure with connected inter-splat pores in each layer. The predicted elastic modulus in out-plane direction agreed well with a wide variety of experimental data (Ref 41-44). Unfortunately, intra-splat cracks were not yet taken into account in this model, and the resulted in-plane modulus of PS ceramic coatings would behave as the corresponding bulk materials. This is obviously far from experimental data.

In this work, a modified model with connected pore structure (connected inter-splat pores and intra-splat cracks) was developed based on lamellar structure with intra-splat cracks. Elastic moduli in both out-plane direction and in-plane direction obtained from modeling were compared with experimental results with an aim at fundamentally understanding the influence of intra-splat cracks on the coating modulus. This would provide further possibility to tailor the microstructure of top-coat for en-
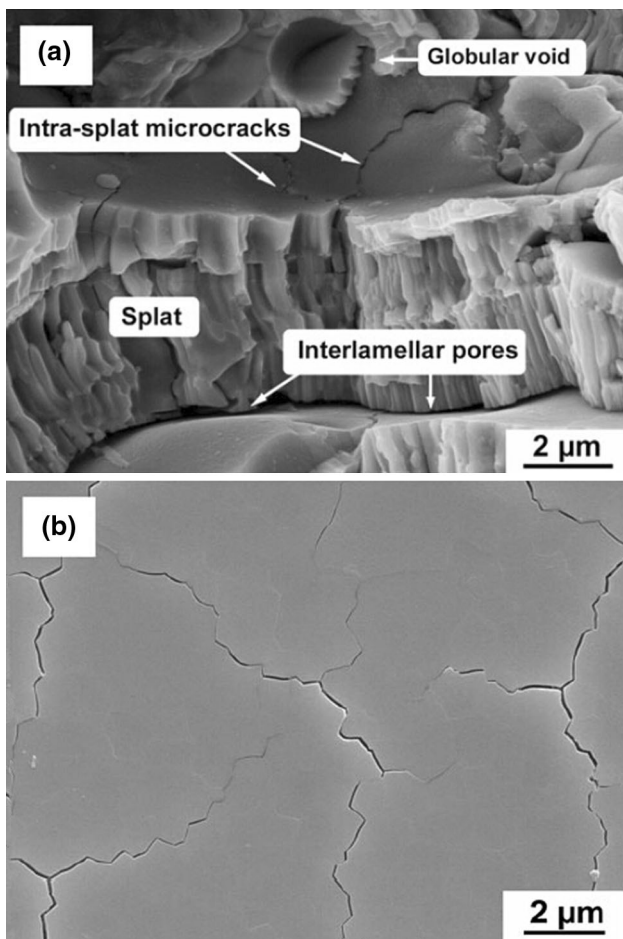
hanced mechanical properties towards the development of advanced TBCs.

2. Framework of the Model

2.1 Model Development

The structure of thermally sprayed ceramic coatings typically modeled by Li et al. (Ref 40) is shown in Fig. 2. In this model, disk-shaped splats with thickness of 1-3 μm stacked together, which are presented clearly from the plan view of lamellar interface (Fig. 2a, in which 2R refers to the diameter of a single splat resulting from a molten droplet, 2a refers to the diameter of bonding area between two splats) and the cross section of coating (Fig. 2b). The limited bonding ratio (the ratio of bonded inter-splat area to the whole splat interface) results in the formation of inter-splat pores.

The essential features of PS ceramic coatings can be summarized as follows: (i) lamellar structure with inter-splat pores in in-plane direction, (ii) intra-splat cracks in out-plane direction (the original disk-shaped splat is divided into small segments by intra-splat cracks), and (iii) connected pores system of inter-splat pores and intra-splat cracks. As a result, the basic unit composing the whole coating is divided in segments by intra-splat cracks. In order to capture these features, similar to the model of Xie et al. (Ref 24), this study follows the cubic unit (termed as structural unit in following text) based on the splat segment divided by intra-splat cracks, as shown in Fig. 3. The structural parameters of a structural unit include length (C), thickness (δ), and bonding ratio (α, which can be obtained by the ratio of bonding area πa^2 to segment area C^2). As a detailed demonstration, Fig. 3(a) shows the

idealized single layer composed of basic structural unit with corresponding structural parameters based on a sprayed single splat, Fig. 3(b) shows the stacked pattern of three layers aiming at presenting the bonding positions of a structural unit with other units in upper and lower layers (U1, U2, U3, U4 refer to the structural units in upper layer, while L1, L2, L3, L4 are structural units in lower layer), and Fig. 3(c) shows the plan view of the structural unit including bonding region with upper and lower layers.

In the present model, the structural unit is the basic unit to compose the whole structure, just like the fact that the splat segment works as the basic unit to compose the

Fig. 3 Modified structural model for PS ceramic coating. (a) An idealized single layer based on a sprayed single splat composed of basic structural unit with corresponding structural parameters, (b) the stacked pattern of three layers, and (c) plan view of structural unit including bonding areas. The blue-filled-cylinders, red-filled cylinders, and black-filled cylinders refer to the bonding area of upper layer (blue cubes of U1, U2, U3, and U4), structural unit (red cube) and lower layer (black cubes of L1, L2, L3, and L4), respectively. 2a, C, and δ refer to the diameter of splat bonding area, length, and thickness of segment, respectively. In order to show clearly stacking mode of upper layer and structural unit without mixing, the bonding areas locating at the bottom centers of L1 and L3 are not shown (Color figure online)

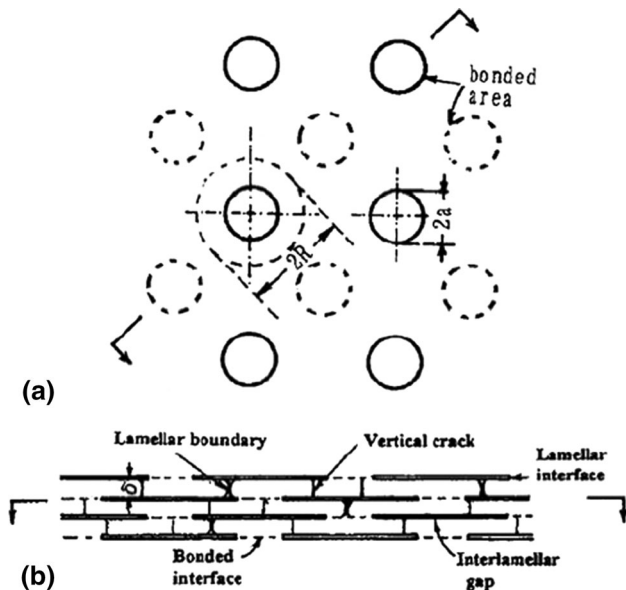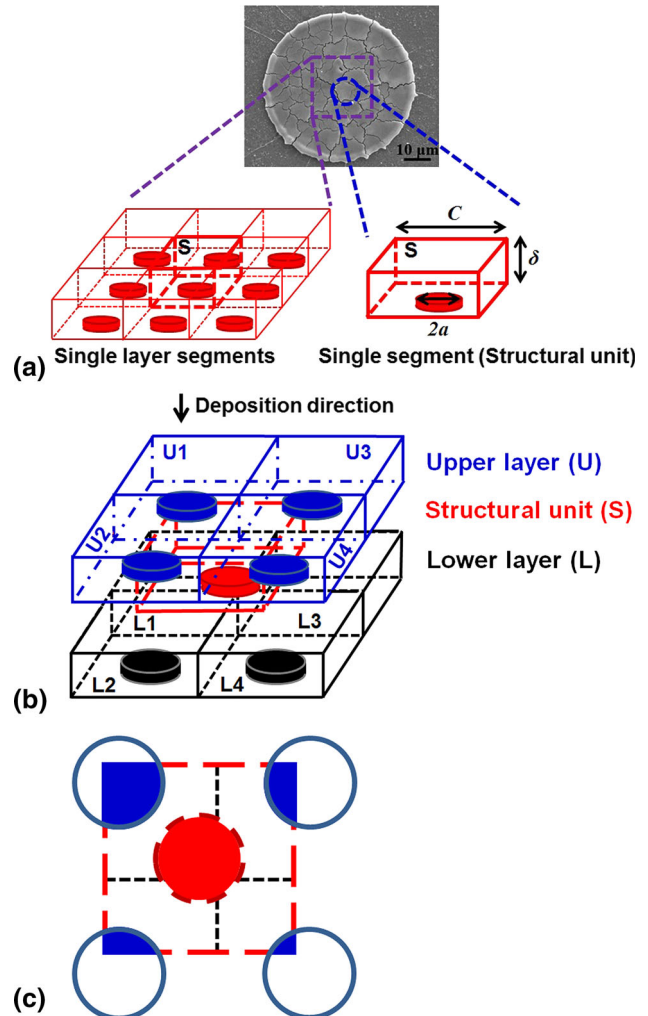**Fig. 2** Idealized model of PS ceramic coating structure (Ref 40): (a) plan view of lamellar interface and (b) cross section of coating

whole coating. The assumptions are as follows: (i) all structural units are assumed to be of cubic shape with the same parameters including unit length and unit thickness (same as splat thickness), (ii) the bonding area between one structural unit and the under layer is located at the bottom center of the structural unit, (iii) the structural units are randomly stacked on the lower layer, and (iv) the structural units in upper layer keep the same in-plane position with those in lower layer, namely U1, U2, U3, U4 are obtained by moving up L1, L2, L3, L4 perpendicularly. Based on these assumptions, every structural unit has the same bonding conditions in top surface and bottom surface, as shown in Fig. 3(c). Accordingly, the structural units in each layer are exactly the same, which result in the composed layers are always the same perpendicular to the deposition direction. However, due to the assumption (iii) mentioned above, the structural units in neighboring layers are not always corresponding with each other along the deposition direction. For example, the S in Fig. 3(b) cannot be obtained by moving L directly along deposition direction. Since the U and L have the same in-plane position, the two-layer-bonded structure, such as S-L, will be much easier to work as the periodic unit to make up the whole coating.

2.2 Boundary Conditions

The calculation of elastic modulus was carried out by Abaqus. Due to the periodic symmetry of the idealized structure in this model (Fig. 3b), any periodic part can be used to calculate the macroscopic properties with periodic boundary conditions. To simplify the calculation, a periodic pattern was used in this model as a calculating unit, where a whole upside structural unit (S) stayed with four parts of downside structural units (L1, L2, L3, and L4), as shown in Fig. 4(a). The calculating unit was obtained by cutting L1, L2, L3, and L4 along the boundary of structural unit in the deposition direction, so L1′, L2′, L3′, and L4′ are the divided parts of L1, L2, L3, and L4, respectively. The A, B, C, D and A′, B′, C′, D′ refer to green points in sections of L2′ and L1′, respectively. Figure 4(b) presents the arrangement of full structure in Abaqus with ten layers stacking for calculation in a particular case termed as uniform distribution, which means that the bonding area in the bottom of a structural unit possesses equal areas of four lower segments, as shown in Fig. 4(c). Due to the periodic properties, the A-B-C-D cross section of L2′ will have consistent deformation behavior with the A′-B′-C′-D′ cross section of L1′, because they are bonded together. The conditions are the same with cross sections in L3′ and L4′. Periodic boundary condition was introduced to the cross section of lower layer to make sure corresponding strain behavior under stress is totally same (assuming no debonding occurred during applying load). The detailed procedure of periodic boundary condition can be acquired referring to Zhang and Wang (Ref 45).

In out-plane direction, the stacking of calculating unit also brings about the same strain behavior for corresponding black and blue bonding area. However, meshing on three-dimensional structure with circle area makes it
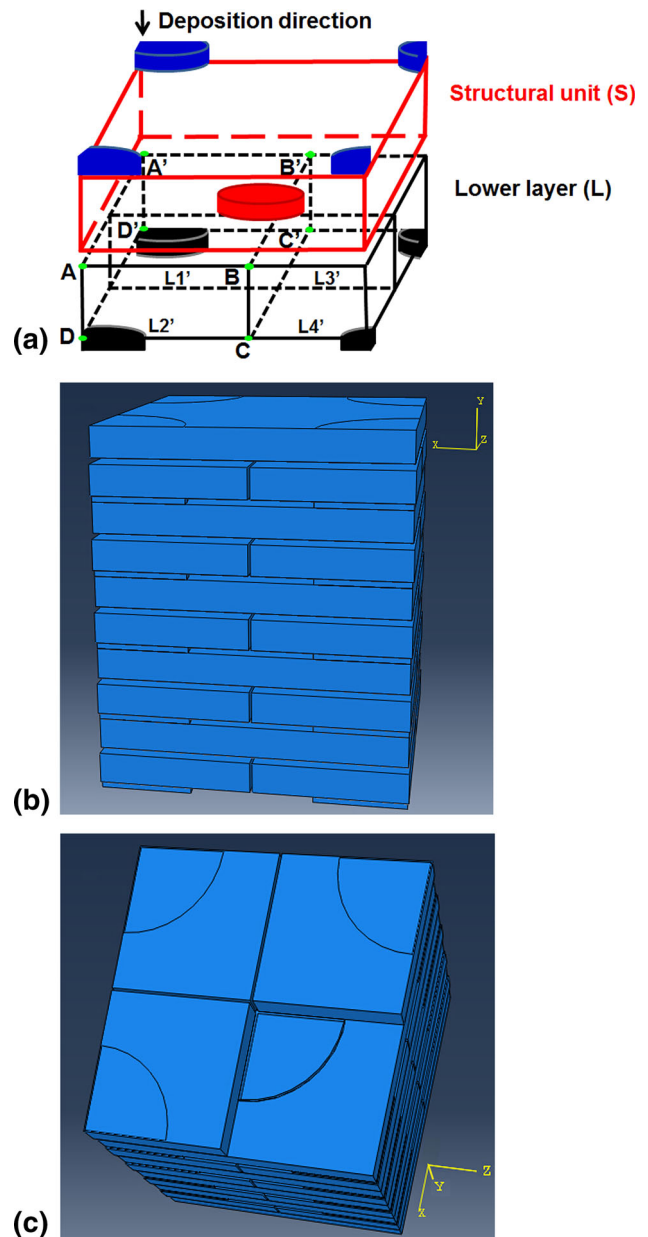

Fig. 4 Structural model of this study. (a) The schematic diagram of a calculating unit extracted from Fig. 3b, in which L1′, L2′, L3′, and L4′ are the divided parts of L1, L2, L3, and L4, respectively. The A, B, C, D and A′, B′, C′, D′ refer to green points in sections of L2′ and L1′, respectively. (b) The arrangement of full structure in Abaqus with ten layers stacking in uniform distribution. (c) The reverse side of uniform distribution with one part missing

difficult to introduce periodic boundary condition. Thus, ten layers (5 calculating units) were chosen to approach it (Fig. 4b). At bonded area, the parts get together with the Tie constraints. At non-bonded area including intra-splat cracks, the contact interaction property was set as Hard contact allowing separation after Surface-to-Surface contact. During meshing, the element shape was set as Tet with standard element library, and the size of global seeds was 0.25 μm. All parts of the calculating unit were set as
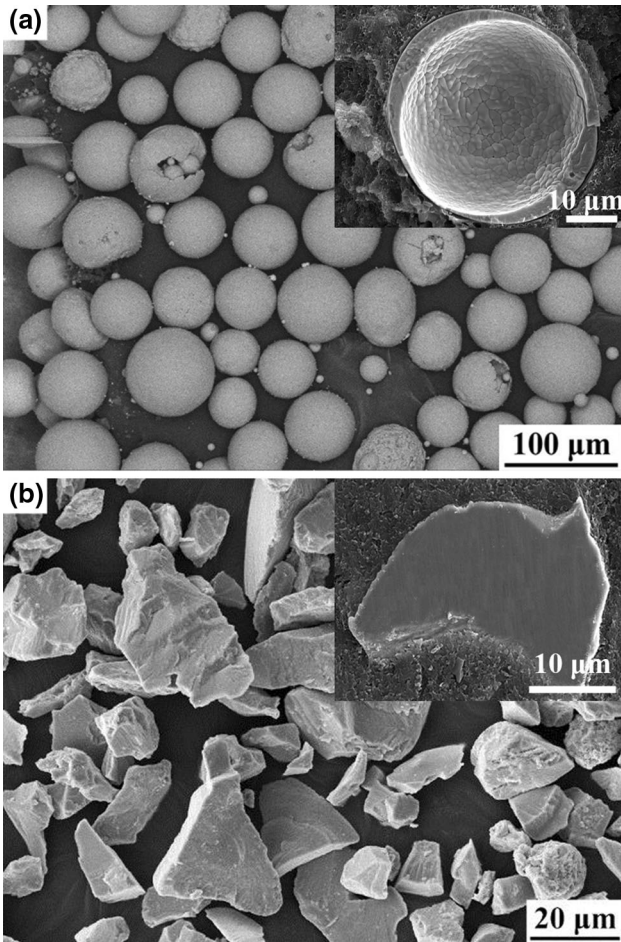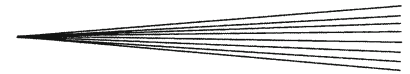
Fig. 5 Surface morphologies of 8 wt.% YSZ powders: (a) HOSP; (b) FC. The inset in (a) exhibits the hollow feature of HOSP powder by cross section. The inset in (b) shows the dense structure of FC powder by cross section

Table 1 Parameters of atmospheric plasma spraying

Parameters	Values
Plasma arc voltage, V	70
Plasma arc current, A	600
Flow rate of primary gas (Ar), L/min	50
Flow rate of secondary gas (H$_2$), L/min	7
Flow rate of powder feeding gas (N$_2$), L/min	7
Spray distance, mm	80
Torch traverse speed, mm/s	800

providing valid support to achieve structure tailoring for better performance. Accordingly, two types of commercial 8 wt.% YSZ powder with very different size distribution were used to obtain relatively reasonable and broad ranges of parameters. One type of YSZ powder is hollow spheroidized powder (HOSP, −75 to + 45 μm, Metco 204B-NS, Sulzer Metco Inc., New York, USA, as shown in Fig. 5a), and the other is fused-crushed powder (FC, 5-22 μm, Fujimi, Aichi, Japan, as shown in Fig. 5b). They were both sprayed on stainless steel substrate to get YSZ coatings using a commercial plasma spray system (GP-80, 80 kW class, Jiujiang, China). The insets in Fig. 5 indicate that the powder structure of FC is solid with dense particle packing, while the HOSP is hollow with loose particle packing and a larger surface area. Compared with the HOSP powders, it is quite easier for the FC powder to get complete single splats with little splashing. This will facilitate in obtaining the accuracy of segment length and thickness. Accordingly, besides the coating deposition, the FC powders were also deposited onto the polished YSZ-sintered ceramic substrate with a preheated temperature of 400 °C to acquire complete single splats aiming at decreasing the difficulty of estimation for the thickness and size of splat segments. The plasma spray parameters are shown in Table 1.

The surface and cross-sectional morphologies of YSZ (including coating and single splats) were observed using scanning electron microscopy (SEM, TESCAN MIRA 3, Czech). The elastic modulus in both directions was measured by Knoop indentation (KI for short, BUEHLER MICROMET 5104, Akashi Corporation, Japan) (Ref 16) at a test load of 300 g holding for 30 s.

homogeneous solid. The Young's modulus and Poisson's ratio of fully dense YSZ were taken as 205 GPa and 0.23 (Ref 46), respectively.

The x-z plane was taken as the reference plane which is perpendicular to the deposition direction. To obtain elastic modulus in out-plane direction (y-axis, i.e., deposition direction), the displacement was applied on bonding area. While for in-plane direction, the x-axis and z-axis will show consistent elastic behavior due to the symmetry of the structure. In this study, the displacement was applied on cross section area along x-axis, and then the stress-strain curve can be obtained through the curve of reaction force and displacement.

3. Experimental Procedure

As a beforehand work, it is necessary to determine the proper ranges of structural parameters for the typical plasma-sprayed YSZ coating to explore the influence of structural parameters on elastic modulus, which aims at

4. Results and Discussion

4.1 Determination of Segment Parameters

The segment thickness (δ) was measured from the cross sections of both sprayed YSZ coatings and single splats. For the YSZ coatings, both fractured cross sections and polished cross sections are shown in Fig. 6 and 7, in which the inseted figures refer to the magnified regions marked in red thinner boxes. Lamellar structure can be clearly observed in both coatings deposited with different powders. A global view of lamellar thickness can be obtained roughly with a broad range. However, besides some splats with a thickness of 0.5-2 μm, some other much thicker
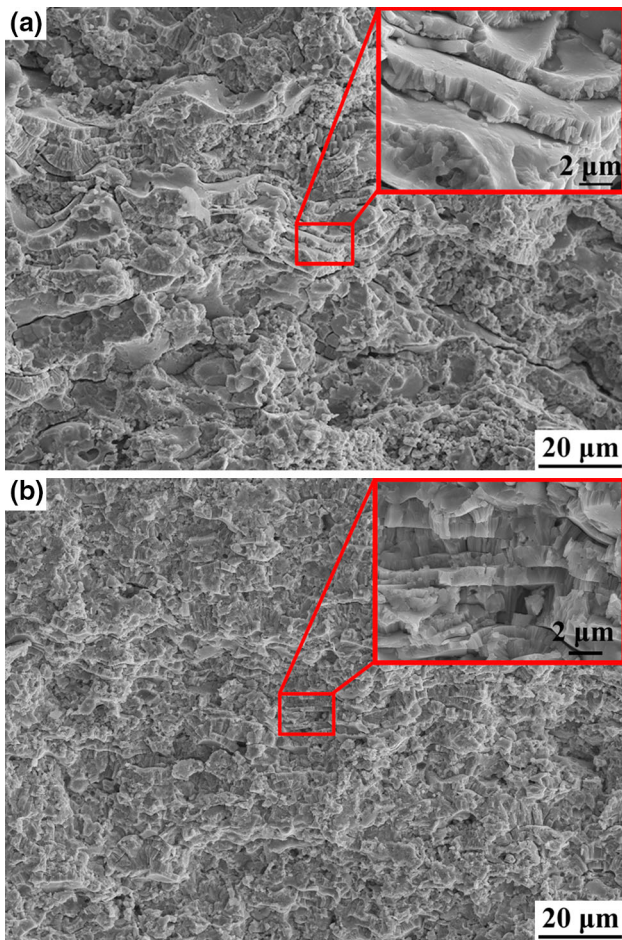
Fig. 6 The morphology of fractured cross section of YSZ coatings deposited with different powders: (a) HOSP and (b) FC. The inseted figures refer to the magnified regions marked in red thinner boxes (Color figure online)

Fig. 7 The polished cross section of YSZ coatings deposited with different powders: (a) HOSP and (b) FC. The inseted figures refer to the magnified regions marked in red thinner boxes (Color figure online)

lamellae can also be found in Fig. 6 and 7. Although the thicker lamellae might result from the bonding between individual splats, it is quite difficult to accurately distinguish individual splats. Therefore, it is more appropriate to examine the splat thickness from the cross sections of individual splats deposited on polished substrate surface to further confirm the rationality of range obtained from coating cross sections, as shown in Fig. 8 with different splat thickness (0.8-1.2 μm (a) and ~1.4 μm (b)), in which the inseted figures refer to the magnified regions of thinner red boxes. It can be clearly found from Fig. 8 that the splat thickness is mainly ranged in 1-2 μm. This result is consistent with previous studies (Ref 47, 48) to quantitatively characterize lamellar structure of plasma-sprayed ceramic coatings.

The surface morphologies of YSZ coatings and single splats are used to examine the segment shape and length (C), as shown in Fig. 9. In detail, Fig. 9(a) and (b) refer to coatings deposited with HOSP powder and FC powder, respectively. Figure 9(c) refers to a single splat deposited with FC powder. Some clear splats can be distinguished from Fig. 9(a)-(c), although rough surface morphologies were
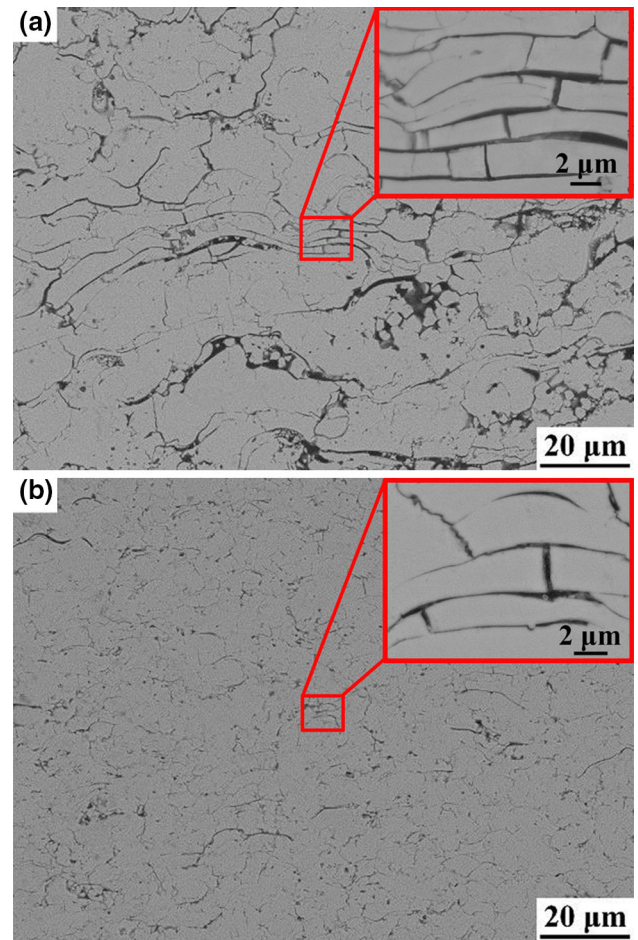
primarily observed from coating surface. The disk-shaped splats were divided into small segments by the intra-splat cracks. The intra-splat cracks proceed randomly in direction, and thereby the segments presented irregular shapes. Considering the assumptions of cubic segment, the average length (C) of segments can be obtained from Eq 1 (Ref 49), in which an apparent area of fixed region (100×100 μm^2 for coating surface and circle splat area for single splats) was divided by amount of segments to get an assumed square area (C^2). The average length of segments obtained from single splats and coating surface was shown in Fig. 10. It can be found that the average length of the segment in single splats was about 7-10 μm, which was smaller than the results obtained from coating surface (about 10-16 μm) in in-plane direction despite of powder types.

$$C = \sqrt{\frac{A}{N}}, \qquad \text{(Eq 1)}$$

where C refers to the average length of a segment, A refers to the apparent area of a fixed region, N refers to the amount of segments in the fixed region.
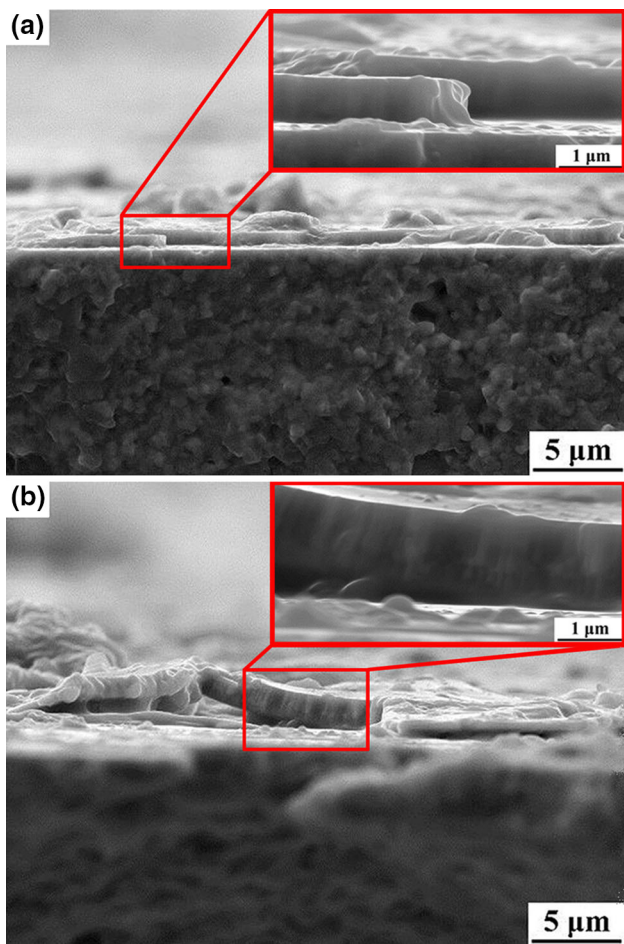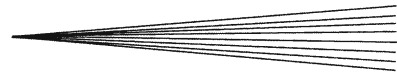
Fig. 8 The morphology of fractured single YSZ splats on polished YSZ substrate surface with different thickness: (a) 0.8-1.2 µm and (b) ~1.4 µm. The inseted figures refer to the magnified regions marked in thinner red boxes (Color figure online)

The discrepancy between the test results acquired from single splats and from coating surface may be attributed to the variation of substrate surface conditions. The single splat was obtained by spraying powder on polished substrate with elevated temperature. While, for the deposition of top layer (coating surface) without preheating, the substrate was the pre-deposited splats which present a rough morphology with un-melted powders inclusion (Ref 50). On the one hand, both the rough surface acting as the substrate for the top layer deposition and the lower depositing temperature result in a lower bonding ratio (Ref 51). On the other hand, the rough surface dispersed the force of solidification contraction leading to intra-splat cracks. As a result, the crack network in a single splat was denser than in coating surface. In other words, the segments divided by intra-splat cracks in a single splat were smaller than those on the coating surface.

The powder size of FC (5-22 µm) is much smaller than HOSP (45-75 µm). However, the powder structure of FC is dense, while the powder structure of HOSP is hollow with loose particle packing and a larger surface area. This indicates that these two kinds of powders with size dif-
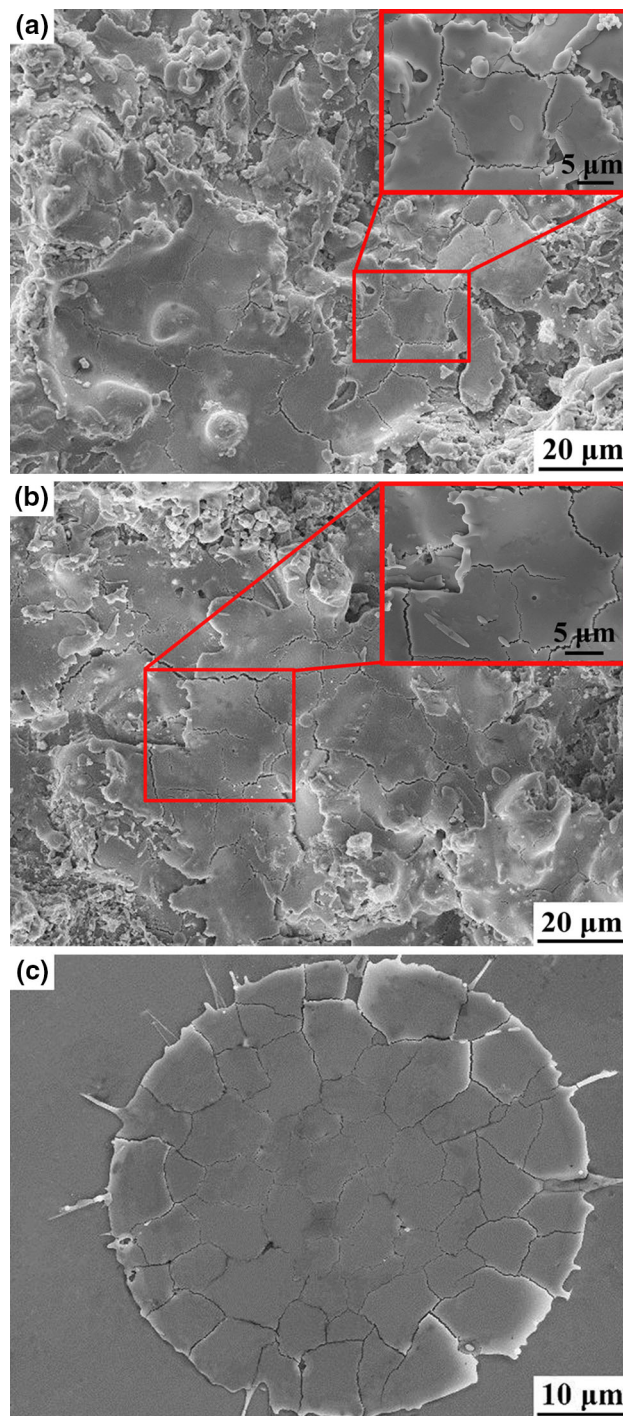

Fig. 9 The surface morphology of YSZ coatings and a single splat. (a) YSZ coating deposited with HOSP powder, (b) YSZ coating deposited with FC powder, and (c) a single splat sprayed on polished YSZ substrate by using FC powder. The inseted figures in (a) and (b) refer to the regions marked in red thinner boxes, respectively (Color figure online)

ference actually have rather commensurate volumes. Considering that the melting process of powder by plasma is mainly based on surface heating, the size difference of molten droplets between HOSP and FC is not so obvious.
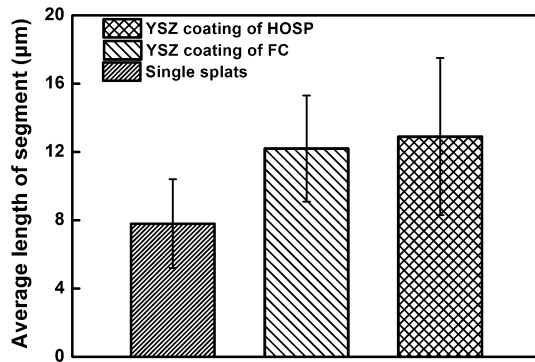
Fig. 10 The average length of segments obtained from single splats and YSZ coating surface deposited with HOSP and FC powders
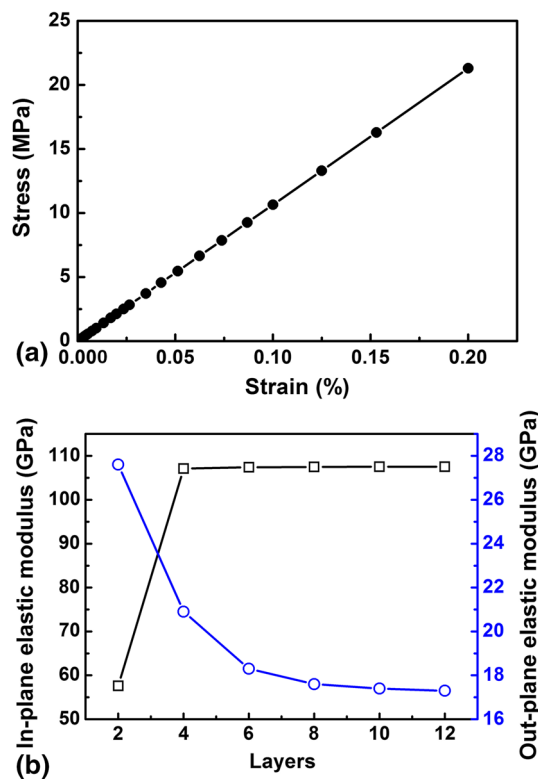

Fig. 11 The stress-strain curve and the obtained elastic modulus with varying layers stacking. (a) The stress-strain curve in in-plane direction along *x*-axis under the condition of 10 μm length, 1 μm width, and 28% bonding ratio with ten layers stacking. (b) The elastic modulus vary with stacking layers in both directions

Therefore, there is no significant difference on the size of segments between these two coatings from the view of splats.

For inter-segment bonding ratio, papers (Ref 9, 13, 47, 48) focusing on structure visualization of plasma-sprayed alumina coating have revealed a bonding ratio range of 10-32% without special substrate preheating. The visualization of void structure of plasma-sprayed YSZ coating also yielded a similar bonding ratio range of 10-32%. Some bonding

ratio-dependent properties, such as fracture toughness in terms of critical strain energy release rate of plasma-sprayed alumina coating (Ref 13, 52) and ionic conductivity of plasma-sprayed YSZ at room temperature (Ref 53), were about 20-30% compared with corresponding bulk materials, which was consistent with the bonding ratio mentioned above. As a consequence, a bonding ratio of 20-36%, a thickness of 0.8-1.6 μm, and a length of 8-16 μm were chosen to set as the ranges of structural parameters to reveal their influence on elastic modulus.

4.2 Influence of Unit Structural Parameters

To examine the influence of structural parameters on elastic modulus in both directions, the uniform distribution of bonding areas was chosen to reveal these trends. As a preliminary work, the stress-strain curve in in-plane direction along *x*-axis under the condition of 10 μm length, 1 μm width, and 28% bonding ratio is shown in Fig. 11(a), from which the elastic modulus can be obtained. The elastic modulus in both directions varying with stacking layers were shown in Fig. 11(b). No obvious variation in the elastic modulus is observed after ten stacking layers (5 calculating units), which validates the choice of ten layers to approach periodic conditions in out-plane direction. This way of linear behavior of stress-strain can be applied to other conditions with different parameters to get elastic modulus. The effect of structural parameters on elastic modulus was shown in Fig. 12 demonstrated with (a) bonding ratio, (b) thickness, and (c) length. It can be seen that the elastic moduli in both directions become larger (Fig. 12a) with the increase of the bonding ratio when the length and thickness were set as 10 and 1 μm, respectively. The thickening of splat segment with a constant bonding ratio of 28% and a constant length of 10 μm leads to a nearly linear decrease of elastic modulus in in-plane direction and a nearly linear increase in out-plane direction (Fig. 12b). The lengthening of segment with a constant bonding ratio of 28% and a constant thickness of 1 μm results in a decrease of elastic modulus in both in-plane direction and out-plane direction (Fig. 12c).

For structural units stacking with uniform distributed bonding areas as shown in Fig. 4(b) and (c), the bonding areas were located at the center of bottom surface and four corners of top surface. During the loading procedure, the bonding areas transmit load among structural units, while the free parts without the constraint of bonding area play a dominant role on the whole deformation.

In addition, strain tolerance, which is related to the structure and material, characterizes the comprehensive deformation without much damage. Excellent strain tolerance often relies on low elastic modulus (Ref 12, 14). Decrease in bonding ratio reduces the connection extent between segments, while lengthening and thickening of segment enlarge the distance of bonding areas between neighboring layers in in-plane direction and out-plane direction, respectively. All these facts increase free part to behave without constraint and enhance strain tolerance, which leads to the drop of elastic modulus in in-plane direction.
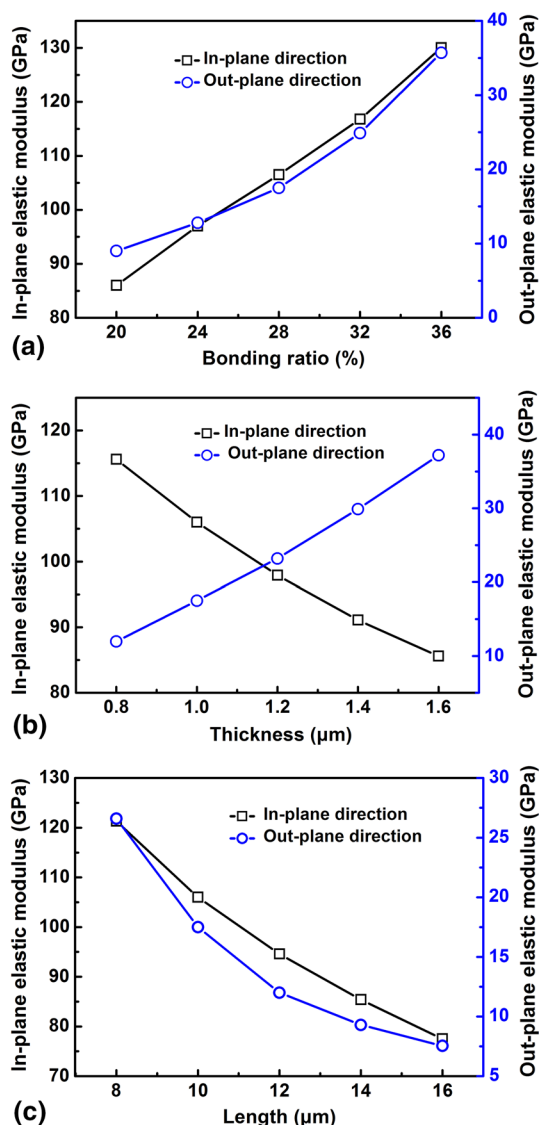
Fig. 12 Effect of structural parameters on elastic modulus: (a) the bonding ratio by fixing length as 10 μm and thickness as 1 μm, (b) the thickness by fixing bonding ratio as 28% and length as 10 μm, and (c) the length by fixing bonding ratio as 28% and thickness as 1 μm

For out-plane direction, the load applying leads to bending of segment between the bonding areas in top and bottom surface, which results in the fact that the bending strain at non-bonded areas plays an essential role on elastic modulus in out-plane direction (Ref 40). Thickening of segment increases the difficulty of bending under load. Increasing the bonding ratio or decreasing the length of segment shortens the distance between the bonding areas in neighboring layers, which leads to the decrease of bending moment and increase of elastic modulus in out-plane direction. It can also be found from Fig. 12 that the inter-splat pores, whose orientation is mostly parallel to the substrate, also have significant influence on elastic modulus in in-plane direction besides out-plane direction. Similarly, the intra-splat cracks show the dependence of

coating modulus on not only their corresponding vertical direction (in-plane direction), but also their parallel direction (out-plane direction). This means that a connected pore system including inter-splat pores and intra-splat cracks is necessary to estimate the effective modulus in both directions.

For TBCs deposited on the Ni-based super alloy, the mismatch of thermal expansion coefficient between coating and substrate during thermal exposure results in in-plane strain perpendicular to the deposition direction (Ref 54). The excellent strain tolerance is necessary to help TBCs in baring certain strain without much damage on structure. It can be found from Fig. 12 that the moderate reduction in bonding ratio, thickening, and lengthening of segments will result in the drop of elastic modulus in in-plane direction. This may provide some supports to tailor plasma-sprayed TBCs with better performance.

4.3 Comparison Between the Model Prediction and Experimental Results

As mentioned above, the inter-splat bonding ratio has obvious influence on elastic modulus in both directions. In addition, the bonding area distribution also affects the strain tolerance in this model. If the uniform distribution of bonding areas is set as the initial state, then possible representative positions of bonding area will be located in a region marked by triangle ABC due to the fact that the symmetry of structure results in the same behavior when bonding area moves out of triangle ABC, as shown in Fig. 13(a). The distribution of bonding area starts from moving along the BA line and ends in moving along the BC line, which will lead to the least and the most influence on elastic modulus, respectively. For example, Fig. 13(b) shows the structural unit resulting from bonding area moving along the BC line in plane-view. The corresponding elastic modulus (fixing length, thickness, and bonding ratio as 10 μm, 1 μm, and 28%, respectively) in in-plane direction along *x*-axis (Fig. 13c) and out-plane direction along *y*-axis (Fig. 13d) clearly showed that the uniform distribution of bonding areas leads to the highest value in in-plane direction and the lowest value in out-plane direction. Because the uniform distribution of bonding areas results in the strongest connection of segments, the largest elastic modulus is obtained in in-plane direction. The moving of bonding area relaxes the connection of segments to a certain extent and enhances strain tolerance, which leads to a lower elastic modulus in in-plane direction. On the contrary, as shown in Fig. 13(b), the uniform distribution of the bonding areas results in the largest distance (R0) without bonding constraint in in-plane direction. This means the easiest bending deformation and the smallest elastic modulus in out-plane direction could be achieved (Fig. 13d). As the centers of the bonding areas gradually move to each other, the distance of the free bending region decreases correspondingly (Fig. 13b, R0 > R1 > R2 > R3), which makes the bending become harder and harder when applying a load in out-plane direction. As a result, the strain tolerance reduces and elastic modulus increases in out-plane direc-

tion (Fig. 13d). The limit position, which means that the centers of bonding areas in neighboring layers are totally coincident, would result in absolute relaxation for structural units in in-plane direction by intra-splat cracks. In other words, there is no connection between the structural units in one layer, because the bonding area will be located at the top center of the lower structural unit rather than at the intra-splat cracks. From the view of whole structure, the intra-splat cracks in every layer will be connected directly in out-plane direction at limit position. This is similar to the structure produced by plasma-spraying physical vapor deposition (PS-PVD) (Ref 55, 56) if the width of columnar equals to segment length. When the structural units remove connection, the strain tolerance in in-plane direction will be increasing apparently. However, the through-thickness cracks obtained by connection of intra-splat cracks will enhance the possibility of coating debonding and reduce the durability of TBCs (Ref

57, 58). What is worse, this would also decrease the coating toughness, while increase the tendency of coating spallation. For out-plane direction, the elastic modulus of limit position will be directly related to the bulk YSZ and bonding ratio.

For the final results, average values of random distributed bonding areas in triangle ABC can be obtained to compare with experimental results. Figure 14 shows the comparison between model prediction and experimental results from both references and present work with (a) in-plane direction and (b) out-plane direction. It can be seen that the model captures the main elastic modulus range for PS-YSZ in both in-plane direction and out-plane direction. Among these results, the results obtained by the resonant ultrasound spectroscopy (a non-destructive technique with excluding the effect of inelastic behavior caused by opening of cracks (Ref 18)) step closer to this work, because both reflect the very essential influence of
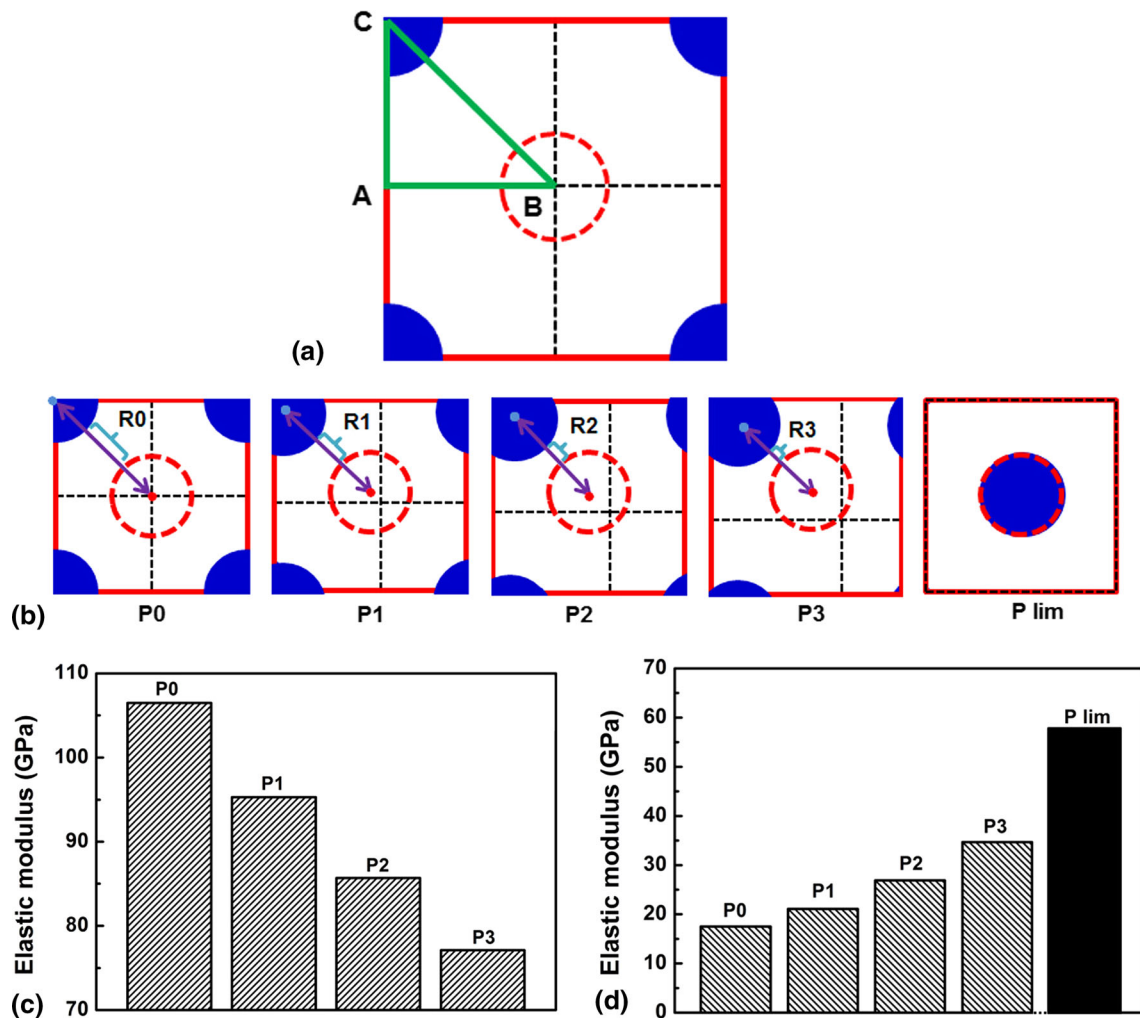

Fig. 13 The random distribution of bonding areas and the corresponding elastic modulus. (a) The representative region (green triangle ABC) of bonding areas distribution with a plane-view of structural unit in Fig. 3(b), (b) the structural unit in plane-view resulting from bonding areas moving along BC, (c) the corresponding elastic modulus in in-plane direction, and (d) the corresponding elastic modulus in out-plane direction. The red points stand for the centers of red circles, the blue points stand for the centers of blue circles, the pink arrows stand for the distance of bonding area centers between red and blue circles. R0, R1, R2, and R3 stand for the distances free from bonding to deform without constraint (Color figure online)
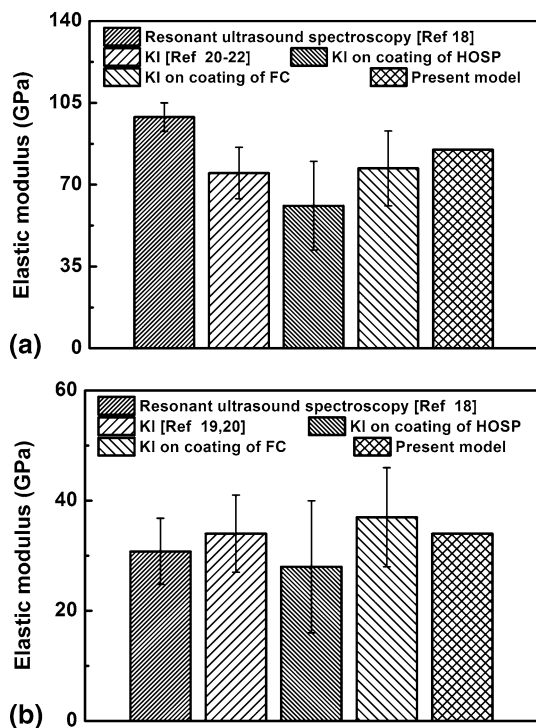
Fig. 14 Comparison between model prediction and experimental results: (a) in-plane direction and (b) out-plane direction

Fig. 15 The comparison of elastic modulus normalized by bulk material in in-plane direction between referenced models (Ref 25, 26, locating at the left side of the red solid line) and the present model locating at the right side of the red solid line. The normalized experimental data acquired from both several references and this study were also introduced for comparison, as shown in left side (Ref 59) and right side (Ref 18, 20-22 and this study) of the red solid line, respectively (Color figure online)

inter-splat pores connected with intra-splat cracks. The Knoop indentation results from references were also consistent with this study, because its indentation scale is several times (about 70-100 μm) of the splat segments (Ref 19-22) and thus a good measurement based on the connection of splat segments can be obtained. As shown in Fig. 7, though lamellar structure with connected pores system can be found in both coatings with high magnification, the coating deposited by HOSP shows some larger scale cracks in both directions compared with coating deposited by FC powders. Apparently, the coating deposited with FC powders shows essential structure of PS-YSZ in most region, which means that inter-splat pores connected with intra-splat cracks play a dominant role on strain tolerance. However, large-scale cracks act certain effect in HOSP coating. Consequently, compared with the YSZ coating deposited with HOSP powders, the experimental values of YSZ coating deposited with FC powders step closer to the model predicted results. Some deviations still exist because the complexity of real structure is still much larger than this idealized model with regular unit shape and flatten stacking lamellae.

4.4 Comparisons Between Models

In Fig. 15, the in-plane elastic modulus normalized by the bulk material acquired from the referenced models (Ref 25, 26), locating at the left side of the red solid line) and the present model locating at the right side of the red solid line were compared. Moreover, the normalized experimental data acquired from both several references and this study
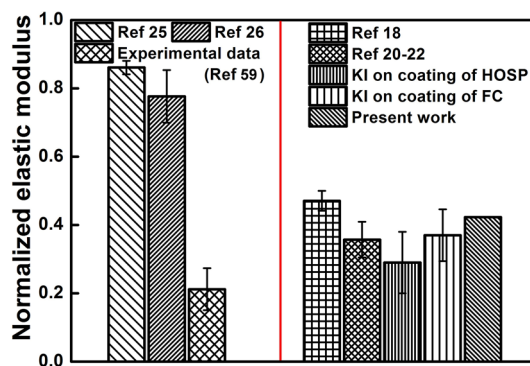
were also introduced for comparison, as shown in left side (Ref 59) and right side (Ref 18, 20-22 and this study) of the red solid line, respectively. It can be found that the model based on lamellar structure with connected inter-splat pores and intra-splat cracks has obvious advantage on the estimation of elastic modulus of PS ceramic coating in in-plane direction compared with indentation measurement results, whose range cannot be captured by the models developed by Kroupa et al. (Ref 25) and Sevostianov et al. (Ref 26) due to neglecting the connection of both flaws. About half more drop compared with bulk materials is also consistent with previous measurement study on elastic modulus of PS ceramic coatings (Ref 18-22). These results further show that the introducing of intra-splat cracks connected with inter-splat pores makes significant contribution to excellent strain tolerance. A view insight into single-splat segments to develop models predicting mechanical and thermal properties (Ref 24) takes a closer step to reveal the essential characteristics of PS ceramic coating. There are also some other important features being neglected, like the unflattened stacking of lamellae and not totally perpendicular or parallel pores, thus a further work may focus on a combination of real structure with FEM and structural models.

5. Conclusions

A modified model based on lamellar structure with connected inter-splat pores and intra-splat cracks was developed to predict elastic modulus in in-plane direction and out-plane direction. Results showed that, by capturing the very essential features of PS-YSZ coatings, the model gave good prediction on elastic modulus in both directions compared with experimental results. Compared with other models, this work also showed obvious advantage on estimating elastic modulus by introducing intra-splat cracks and connected pores system, especially in in-plane direction. On account of

the idealized model unit with length, thickness, and bonding ratio simplified from splat segments, this work also gave the relationship between elastic modulus and structural parameters. Based on this modified model, a more effective and reasonable design on structure of YSZ coatings could be achieved in future, so as to obtain more excellent strain tolerance to undergo thermal exposure.

Acknowledgments

References

1. J.T. Demasimarcin and D.K. Gupta, Protective Coatings in the Gas-Turbine Engine, *Surf. Coat. Technol.*, 1994, **68**, p 1-9
2. T.V.M. Andritschky, W. Fischer, H.P. Buchkremer, and D. Stover, Effects of Deposition Temperature and Thermal Cycling on Residual Stress State in Zirconia-Based Thermal Barrier Coatings, *Surf. Coat. Technol.*, 1999, **120**, p 103-111
3. N.P. Padture, M. Gell, and E.H. Jordan, Thermal Barrier Coatings for Gas-Turbine Engine Applications, *Science*, 2002, **296**(5566), p 280-284
4. M. Matsumoto, H. Takayama, D. Yokoe, K. Mukai, H. Matsubara, Y. Kagiya, and Y. Sugita, Thermal Cycle Behavior of Plasma Sprayed La_2O_3, Y_2O_3 Stabilized ZrO_2 Coatings, *Scr. Mater.*, 2006, **54**(12), p 2035-2039
5. S. Asghari, M. Salimi, and M. Salehi, Modeling Nonlinear Elastic Behavior of Plasma Sprayed Ceramics and Its Evolution with Sintering, *Mater. Sci. Eng. A*, 2010, **527**(16-17), p 4241-4249
6. Y.S. Tian, C.Z. Chen, D.Y. Wang, and Q.M. Ji, Recent Developments in Zirconia Thermal Barrier Coatings, *Surf. Rev. Lett.*, 2005, **12**(3), p 369-378
7. A. Feuerstein, J. Knapp, T. Taylor, A. Ashary, A. Bolcavage, and N. Hitchman, Technical and Economical Aspects of Current Thermal Barrier Coating Systems for Gas Turbine Engines by Thermal Spray and EBPVD: A Review, *J. Therm. Spray Technol.*, 2008, **17**(2), p 199-213
8. C.U. Hardwicke and Y.C. Lau, Advances in Thermal Spray Coatings for Gas Turbines and Energy Generation: A Review, *J. Therm. Spray Technol.*, 2013, **22**(5), p 564-576
9. A. Ohmori and C.J. Li, Quantitative Characterization of the Structure of Plasma-Sprayed Al_2O_3 Coating by Using Copper Electroplating, *Thin Solid Films*, 1991, **201**(2), p 241-252
10. P. Fauchais, M. Fukumoto, A. Vardelle, and M. Vardelle, Knowledge Concerning Splat Formation: An Invited Review, *J. Therm. Spray Technol.*, 2004, **13**(3), p 337-360
11. T.W. Clyne and S.C. Gill, Residual Stresses in Thermal Spray Coatings and Their Effect on Interfacial Adhesion: A Review of Recent Work, *J. Therm. Spray Technol.*, 1996, **5**(4), p 401-418
12. A. Cipitria, I.O. Golosnoy, and T.W. Clyne, A Sintering Model for Plasma-Sprayed Zirconia TBCs. Part I: Free-Standing Coatings, *Acta Mater.*, 2009, **57**(4), p 980-992
13. C.J. Li and A. Ohmori, Relationships Between the Microstructure and Properties of Thermally Sprayed Deposits, *J. Therm. Spray Technol.*, 2002, **11**(3), p 365-374
14. J.A. Thompson and T.W. Clyne, The Effect of Heat Treatment on the Stiffness of Zirconia Top Coats in Plasma-Sprayed TBCs, *Acta Mater.*, 2001, **49**(9), p 1565-1575
15. K.T. Voisey and T.W. Clyne, Laser Drilling of Cooling Holes Through Plasma Sprayed Thermal Barrier Coatings, *Surf. Coat. Technol.*, 2004, **176**(3), p 296-306
16. R.S. Lima, S.E. Kruger, G. Lamouche, and B.R. Marple, Elastic Modulus Measurements Via Laser-Ultrasonic and Knoop Indentation Techniques in Thermally Sprayed Coatings, *J. Therm. Spray Technol.*, 2005, **14**(1), p 52-60
17. S. Guo and Y. Kagawa, Young's Moduli of Zirconia Top-Coat and Thermally Grown Oxide in a Plasma-Sprayed Thermal Barrier Coating System, *Scr. Mater.*, 2004, **50**(11), p 1401-1406
18. Y. Tan, A. Shyam, W.B. Choi, E. Lara-Curzio, and S. Sampath, Anisotropic Elastic Properties of Thermal Spray Coatings Determined Via Resonant Ultrasound Spectroscopy, *Acta Mater.*, 2010, **58**(16), p 5305-5315
19. D.M. Zhu and R.A. Miller, Thermal Conductivity and Elastic Modulus Evolution of Thermal Barrier Coatings Under High Heat Flux Conditions, *J. Therm. Spray Technol.*, 2000, **9**(2), p 175-180
20. H.J. Kim and Y.G. Kweon, Elastic Modulus of Plasma-Sprayed Coatings Determined by Indentation and Bend Tests, *Thin Solid Films*, 1999, **342**(1-2), p 201-206
21. R.S. Lima, A. Kucuk, and C.C. Berndt, Evaluation of Microhardness and Elastic Modulus of Thermally Sprayed Nanostructured Zirconia Coatings, *Surf. Coat. Technol.*, 2001, **135**(2-3), p 166-172
22. S.H. Leigh, C.K. Lin, and C.C. Berndt, Elastic Response of Thermal Spray Deposits Under Indentation Tests, *J. Am. Ceram. Soc.*, 1997, **80**(8), p 2093-2099
23. M. Shinozaki, T.W. Clyne, and A. Methodology, Based on Sintering-Induced Stiffening, for Prediction of the Spallation Lifetime of Plasma-Sprayed Coatings, *Acta Mater.*, 2013, **61**(2), p 579-588
24. H. Xie, Y.C. Xie, G.J. Yang, C.X. Li, and C.J. Li, Modeling Thermal Conductivity of Thermally Sprayed Coatings with Intrasplat Cracks, *J. Therm. Spray Technol.*, 2013, **22**(8), p 1328-1336
25. F. Kroupa and J. Dubsky, Pressure Dependence of Young's Moduli of Thermal Sprayed Materials, *Scr. Mater.*, 1999, **40**(11), p 1249-1254
26. I. Sevostianov and M. Kachanov, Modeling of The Anisotropic Elastic Properties of Plasma-Sprayed Coatings in Relation to Their Microstructure, *Acta Mater.*, 2000, **48**(6), p 1361-1370
27. J.H. Qiao, R. Bolot, and H.L. Liao, Finite Element Modeling of the Elastic Modulus of Thermal Barrier Coatings, *Surf. Coat. Technol.*, 2013, **220**, p 170-173
28. K. Bobzin, N. Kopp, T. Warda, and M. Ote, Determination of the Effective Properties of Thermal Spray Coatings Using 2D and 3D Models, *J. Therm. Spray Technol.*, 2012, **21**(6), p 1269-1277
29. L. Li, N. Hitchman, and J. Knapp, Failure of Thermal Barrier Coatings Subjected to CMAS Attack, *J. Therm. Spray Technol.*, 2010, **19**(1-2), p 148-155
30. P. Mohan, T. Patterson, B. Yao, and Y. Sohn, Degradation of Thermal Barrier Coatings by Fuel Impurities and CMAS: Thermochemical Interactions and Mitigation Approaches, *J. Therm. Spray Technol.*, 2010, **19**(1-2), p 156-167
31. A.D. Gledhill, K.M. Reddy, J.M. Drexler, K. Shinoda, S. Sampath, and N.P. Padture, Mitigation of Damage from Molten Fly Ash to Air-Plasma-Sprayed Thermal Barrier Coatings, *Mater. Sci. Eng. A*, 2011, **528**(24), p 7214-7221
32. J. Wu, H.B. Guo, Y.Z. Gao, and S.K. Gong, Microstructure and Thermo-Physical Properties of Yttria Stabilized Zirconia Coatings with CMAS Deposits, *J. Eur. Ceram. Soc.*, 2011, **31**(10), p 1881-1888
33. J. Wu, H.B. Guo, M. Abbas, and S.K. Gong, Evaluation of Plasma Sprayed YSZ Thermal Barrier Coatings with the CMAS Deposits Infiltration Using Impedance Spectroscopy, *Prog. Natl. Sci. Mater.*, 2012, **22**(1), p 40-47
34. W.S. Li, H.Y. Zhao, X.H. Zhong, L. Wang, and S.Y. Tao, Air Plasma-Sprayed Yttria and Yttria-Stabilized Zirconia Thermal Barrier Coatings Subjected to Calcium-Magnesium-Alumino-Silicate (CMAS), *J. Therm. Spray Technol.*, 2014, **23**(6), p 975-983
35. C.J. Li, C.X. Li, and M.J. Ning, Performance of YSZ Electrolyte Layer Deposited by Atmospheric Plasma Spraying for Cermet-Supported Tubular SOFC, *Vacuum*, 2004, **73**(3-4), p 699-703
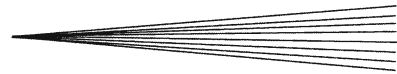
36. C.J. Li, X.J. Ning, and C.X. Li, Effect of Densification Processes on the Properties of Plasma-Sprayed YSZ Electrolyte Coatings for Solid Oxide Fuel Cells, *Surf. Coat. Technol.*, 2005, **190**(1), p 60-64

37. X.J. Ning, C.X. Li, C.J. Li, and G.J. Yang, Modification of Microstructure and Electrical Conductivity of Plasma-Sprayed YSZ Deposit Through Post-densification Process, *Mater. Sci. Eng. A*, 2006, **428**(1-2), p 98-105

38. C. Zhang, W.Y. Li, M.P. Planche, C.X. Li, H.L. Liao, C.J. Li, and C. Coddet, Study on Gas Permeation Behaviour Through Atmospheric Plasma-Sprayed Yttria Stabilized Zirconia Coating, *Surf. Coat. Technol.*, 2008, **202**(20), 5055-5061

39. C.X. Li, C.J. Li, and G.J. Yang, Development of a Ni/Al$_2$O$_3$ Cermet-Supported Tubular Solid Oxide Fuel Cell Assembled with Different Functional Layers by Atmospheric Plasma-Spraying, *J. Therm. Spray Technol.*, 2009, **18**(1), p 83-89

40. C.J. Li, A. Ohmori, and R. McPherson, The Relationship Between Microstructure and Young's Modulus of Thermally Sprayed Ceramic Coatings, *J. Mater. Sci.*, 1997, **32**(4), p 997-1004

41. M. Moss, D.M. Schuster, and W.L. Cyrus, Properties of Filament-Reinforced Plasma-Sprayed Alumina, *Am. Ceram. Soc. Bull.*, 1972, **51**(2), p 167

42. R.C. Tucker, Structure Property Relationships in Deposits Produced by Plasma Spray and Detonation Gun Techniques, *J. Vac. Sci. Technol.*, 1974, **11**(4), p 725-734

43. K.S. Shi, Z.Y. Qian, and M.S. Zhuang, Microstructure and Properties of Sprayed Ceramic Coating, *J. Am. Ceram. Soc.*, 1988, **71**(11), p 924-929

44. N.N. Ault, Characteristics of Refractory Oxide Coatings Produced by Flame-Spraying, *J. Am. Ceram. Soc.*, 1957, **40**(3), p 69-74

45. W.X. Zhang, T.J. Wang, and L.X. Li, Numerical Analysis of the Transverse Strengthening Behavior of Fiber-Reinforced Metal Matrix Composites, *Comput. Mater. Sci.*, 2007, **39**(3), p 684-696

46. X.J. Lu and P. Xiao, Constrained Sintering of YSZ/Al$_2$O$_3$ Composite Coatings on Metal Substrates Produced from Eletrophoretic Deposition, *J. Eur. Ceram. Soc.*, 2007, **27**(7), p 2613-2621

47. C.J. Li and W.Z. Wang, Quantitative Characterization of Lamellar Microstructure of Plasma-Sprayed Ceramic Coatings Through Visualization of Void Distribution, *Mater. Sci. Eng. A*, 2004, **386**(1-2), p 10-19

48. Y. Li, C.J. Li, G.J. Yang, and C.X. Li, Relation Between Microstructure and Thermal Conductivity of Plasma-Sprayed 8YSZ Coating, *Int. J. Mod. Phys. B*, 2010, **24**(15-16), p 3017-3022

49. Y.Z. Xing, Y. Li, C.J. Li, C.X. Li, and G.J. Yang, Influence of Substrate Temperature on Microcracks Formation in Plasma-Sprayed Yttria-Stabilized Zirconia Splats, *Key Eng. Mater.*, 2008, **373-374**, p 69-72

50. G.J. Yang, C.X. Li, and C.J. Li, Characterization of Nonmelted Particles and Molten Splats in Plasma-Sprayed Al$_2$O$_3$ Coatings by a Combination of Scanning Electron Microscopy, X-ray Diffraction Analysis, and Confocal Raman Analysis, *J. Therm. Spray Technol.*, 2012, **22**, p 131-137

51. G.J. Yang and C.X. Li, S. H, Y. Z. Xing, E. J. Yang and C. J. Li. Critical Bonding Temperature for the Splat Bonding Formation During Plasma Spraying of Ceramic Materials, *Surf. Coat. Technol.*, 2013, **235**, p 841-847

52. C.J. Li, W.Z. Wang, and Y. He, Measurement of Fracture Toughness of Plasma-Sprayed Al$_2$O$_3$ Coatings Using a Tapered Double Cantilever Beam Method, *J. Am. Ceram. Soc.*, 2003, **86**(8), p 1437-1439

53. C. Zhang, C.J. Li, G. Zhang, X.J. Ning, C.X. Li, H.L. Liao, and C. Coddet, Ionic Conductivity and Its Temperature Dependence of Atmospheric Plasma-Sprayed YttriaStabilized Zirconia Electrolyte, *Mater. Sci. Eng. B*, 2007, **137**(1-3), p 24-30

54. A. Cipitria, I.O. Golosnoy, and T.W. Clyne, A Sintering Model for Plasma-Sprayed Zirconia Thermal Barrier Coatings. Part II: Coatings Bonded to A Rigid Substrate, *Acta Mater.*, 2009, **57**(4), p 993-1003

55. G. Mauer, A. Hospach, N. Zotov, and R. Vassen, Process Conditions and Microstructures of Ceramic Coatings by Gas Phase Deposition Based on Plasma Spraying, *J. Therm. Spray Technol.*, 2013, **22**(2-3), p 83-89

56. K. von Niessen and M. Gindrat, Plasma Spray-PVD: A New Thermal Spray Process to Deposit Out of the Vapor Phase, *J. Therm. Spray Technol.*, 2011, **20**(4), p 736-743

57. X.L. Fan, R. Xu, W.X. Zhang, and T.J. Wang, Effect of Periodic Surface Cracks on the Interfacial Fracture of Thermal Barrier Coating System, *Appl. Surf. Sci.*, 2012, **258**, p 9816-9823

58. R. Xu, X.L. Fan, W.X. Zhang, Y. Song, and T.J. Wang, Effects of Geometrical and Material Parameters of Top and Bond Coats on the Interfacial Fracture in Thermal Barrier Coating System, *Mater. Des.*, 2013, **47**, p 566-574

59. M. Vilemova, J. Matejicek, R. Musalek, and J. Nohava, Application of Structure-Based Models of Mechanical and Thermal Properties on Plasma Sprayed Coatings, *J. Therm. Spray Technol.*, 2012, **21**(3-4), p 372-382